



Artificial microtubules for rapid and collective transport of magnetic microcargoes

Hongri Gu^{1,3}✉, Emre Hanedan¹, Quentin Boehler¹, Tian-Yun Huang^{1,4}, Arnold J. T. M. Mathijssen^{1,2}✉ and Bradley J. Nelson¹✉

Directed transport of microcargoes is essential for living organisms as well as for applications in microrobotics, nanotechnology and biomedicine. Existing delivery technologies often suffer from low speeds, limited navigation control and dispersal by cardiovascular flows. In cell biology, these issues are largely overcome by cytoskeletal motors that carry vesicles along microtubule highways. Thus inspired, here we developed an artificial microtubule (AMT), a structured microfibre with embedded micromagnets that serve as stepping stones to guide particles rapidly through flow networks. Compared with established techniques, the microcargo travels an order of magnitude faster using the same driving frequency, and dispersal is mitigated by a strong dynamic anchoring effect. Even against strong fluid flows, the large local magnetic-field gradients enable both anchoring and guided propulsion. Finally, we show that AMTs can facilitate the self-assembly of microparticles into active-matter clusters, which then enhance their walking speed by bridging over stepping stones collectively. Hence, we demonstrate a unique strategy for robust delivery inside microvascular networks and for minimally invasive interventions, with non-equilibrium effects that could be equally relevant for enhancing biological transport processes.

The function of biological systems is inherently limited by fundamental physical laws^{1,2}. Cells rely on diffusion to distribute materials at the microscale, but larger organisms must evoke active transport mechanisms that bridge the diffusive and convective scales, while overcoming viscous dissipation and non-equilibrium effects^{3,4}. A particularly efficient transport mechanism that evolved subject to these constraints is the self-organized motion of molecular motor proteins along cytoskeletal microfibres^{5,6} (Fig. 1a). For example, kinesins can walk along microtubules to drag neurotransmitter vesicles across nerve cells millions of times their own size⁷. To achieve this active transport reliably over long distances, each kinesin motor has two binding groups connected with a flexible joint that can alternately bind and walk on the microtubules using energy from ATP hydrolysis⁸. Their speed (up to about 100 body lengths per second) depends not only on the energy provided (ATP concentration) but also on physical properties, as their architecture must withstand the large Stokesian drag forces⁷. This cargo haulage can also drive cytoplasmic streaming by hydrodynamic entrainment, enhancing the intracellular transport further⁹. Recent advances have enabled the design of engineered molecular motors^{9,10} and artificial microtubules in the context of self-assembled machines^{11–13}, but microrobotic transport along microfilaments (Fig. 1b–d) remains unexplored despite its natural primacy.

Microrobotic delivery technologies are developing rapidly, each with advantages and inherent limitations. Mobile microrobots can propel and navigate in viscous liquid environments, which hold potential for minimally invasive surgery and precision drug delivery inside the human body^{14–18}. However, delivering microcargoes remains challenging owing to their relatively low speed, difficult navigation, and dispersal in complex and dynamic flow environments^{19–24}. Existing methods for microrobotic delivery require high-resolution spatiotemporal tracking with limited capability to

compensate for environmental disturbances, hindering their potential impact in biomedical applications^{25–28}. Tubular medical catheters are widely used for delivering drugs in medicine, and functional microrobot suspensions can be pumped through the inner lumen and delivered to the tip position²⁹. However, catheters are not easily miniaturized to the micrometre scale, and the required pumping pressure increases rapidly with a decreasing inner diameter ($\Delta p \propto 1/R^4$) based on the Hagen–Poiseuille equation. As a result, it is prohibitively difficult to deliver sufficient amounts of drugs through micrometre-sized capillary tubes.

Design and function of artificial microtubules

Inspired by cytoskeletal transport, we present a strategy to convey magnetic microcargoes using structured magnetic microfibres (Fig. 1b), which we called artificial microtubules (AMTs). They are about an order of magnitude thinner than 25 gauge (G25) needles (Fig. 1c) so they can deliver cargo much more accurately (Fig. 1d). Unlike moving inside tube-shaped catheters, the magnetic microcargoes actively propel along the outside of the AMTs (Fig. 2a,b and Supplementary Video 1). This is achieved by embedding a one-dimensional array of magnetic plates (nickel, with 50 μm height, 40 μm width and 15 μm length, and periodicity 90 μm) inside a non-magnetic fibre (SU-8, with 50 μm height, 80 μm width and 20 mm length) using photolithography and electroplating processes (Extended Data Fig. 1 and ‘Fabrication of artificial microtubules’ in Methods). These embedded nickel plates, which we call stepping stones, have a low magnetic coercivity (Extended Data Fig. 2), such that they can be magnetized dynamically by an external rotating magnetic field. Consequently, they generate large local magnetic-field gradients (Fig. 2c) on the surface of the structured fibre, providing anchoring points for the walking magnetic microrobots to mitigate dispersal by external flows or fluctuations without being limited by the Hagen–Poiseuille law.

¹Institute of Robotics and Intelligent Systems, ETH Zürich, Zurich, Switzerland. ²Department of Physics and Astronomy, University of Pennsylvania, Philadelphia, PA, USA. ³Present address: Department of Physics, University of Konstanz, Konstanz, Germany. ⁴Present address: Department of Advanced Manufacturing and Robotics, Peking University, Beijing, China. ✉e-mail: hongri.gu@uni-konstanz.de; amaths@upenn.edu; bnelson@ethz.ch

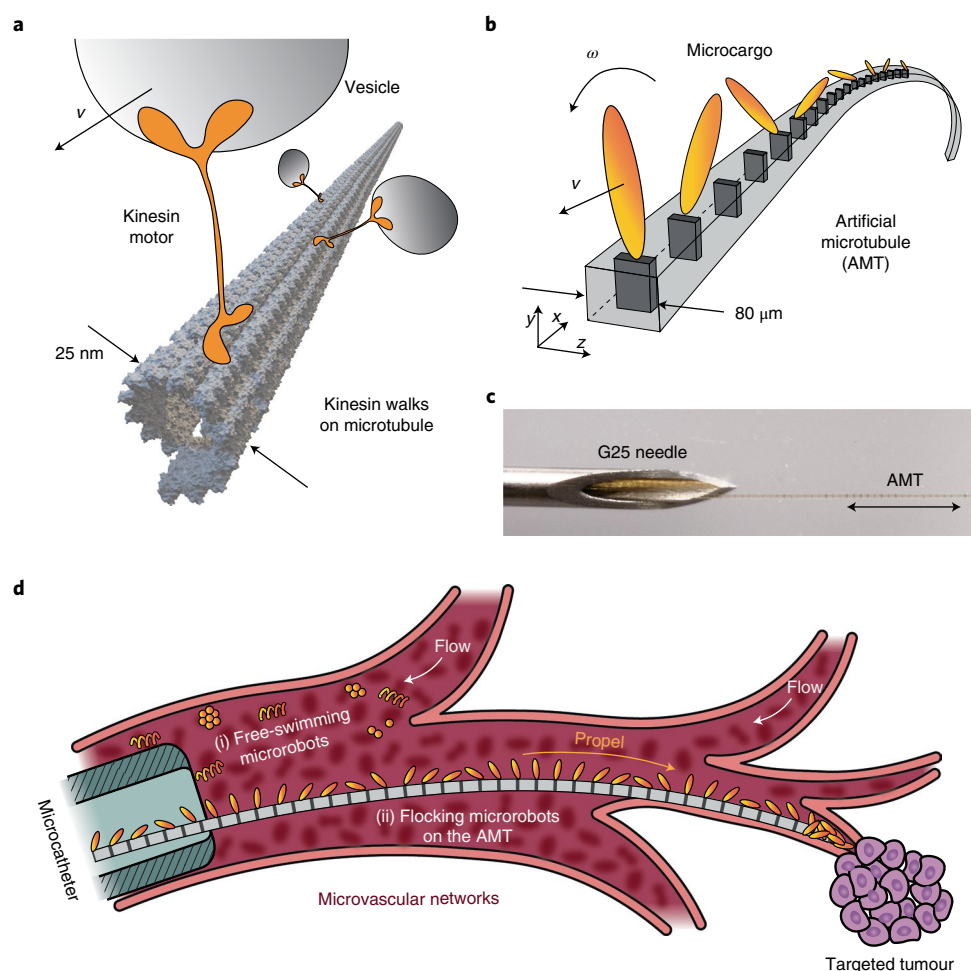


Fig. 1 | Concept of AMTs and potential usage scenario. a, b, Concept: kinesin motor walking on natural microtubules (**a**) compared with microrobots on the AMT (**b**). The linear and rotational velocities of the moving object are marked as v and ω , respectively. **c,** Image of a single artificial microtubule (width 0.05 mm) slides out a 25 gauge needle (outer diameter 0.5 mm , inner diameter 0.26 mm). **d,** A graphical illustration of AMT deployment in microvascular networks. First, a microcatheter (diameter $\sim 0.5\text{ mm}$) is inserted to its limitation, where it cannot enter into smaller vessels. Then, an AMT (diameter $\sim 0.05\text{ mm}$) is pushed through the microcatheter and guided magnetically into a microvascular branch to the targeted tumour. Compared with freely swimming microrobots (i), the transport of microcargoes along the AMT (ii) is faster and more robust due to the magnetic anchoring to the stepping stones, especially against cardiovascular flows.

We first investigated the transport capabilities of the AMTs using a magnetic microrod cargo (nickel, $15\text{ }\mu\text{m}$ width, $90\text{ }\mu\text{m}$ length and $8\text{ }\mu\text{m}$ thickness) in a highly viscous Newtonian liquid (99% glycerol, viscosity 1.15 Pa s). Under a slowly rotating magnetic field B (10 mT , 0.5 Hz in the x - y plane), the long axis of the microrod was aligned and rotated in synchrony with the external magnetic field, as depicted in Fig. 2a,b. Unlike existing mobile microrobots (for example, surface rollers and helical microswimmers), the walkers do not rely on Stokesian hydrodynamic interactions to propel forwards. Instead, the large magnetic-field gradient close to each stepping stone induces a strong attractive force that provides traction to the microrods, akin to molecular motor binding sites (Fig. 2c). As a result, the microrod pivots around the anchoring points and rapidly propels forwards, because it does not slip on the surface (Fig. 2a,b). The microtubule also enhances microrod propulsion. When the magnetic field is parallel to the microtubule, a negative field gradient is generated at the anchoring points such that the microrods are repelled, helping them to release and move to the next anchoring point (Supplementary Video 1). This stepwise walking behaviour is particularly efficient, allowing speeds of up to two body lengths per rotation period, which is more than an order of magnitude faster than flexible and helical microswimmers and surface walkers (Fig. 3c).

We studied the dynamic transport of the same magnetic microrod at different frequencies by tracking its orientation and central position (Fig. 2d). At low frequencies ($f=0.5\text{ Hz}$), the microrod synchronized with the external magnetic field and moved forwards using anchoring points (two steps per rotation). Its centre traced out trajectories of semicircles, showing a strong position and orientation correlation (Fig. 2e and Extended Data Fig. 5). At a higher frequency ($f=2\text{ Hz}$), although the microrod was still rotationally synchronized, it could no longer maintain the translational pace (<2 steps per rotation) owing to increased translational drag force. This can be seen from the pink-to-yellow colour transition periodicity in Fig. 2f, with the centre drawing a flatter line. This translational asynchronized behaviour is referred to as ‘slip-out’, which is comparable to the widely used rotational ‘step-out’ behaviour in rotational asynchronization. At even higher frequencies ($f=4\text{ Hz}$; Fig. 2g), the microrod was both rotationally and translationally asynchronized, which further decreased the translational speed (Supplementary Video 2).

Quantification of transport velocities

To understand the frequency-dependent coupling between translation and rotation, we systematically tested the locomotion speed of the microrods in the same viscous liquid (99% glycerol) using

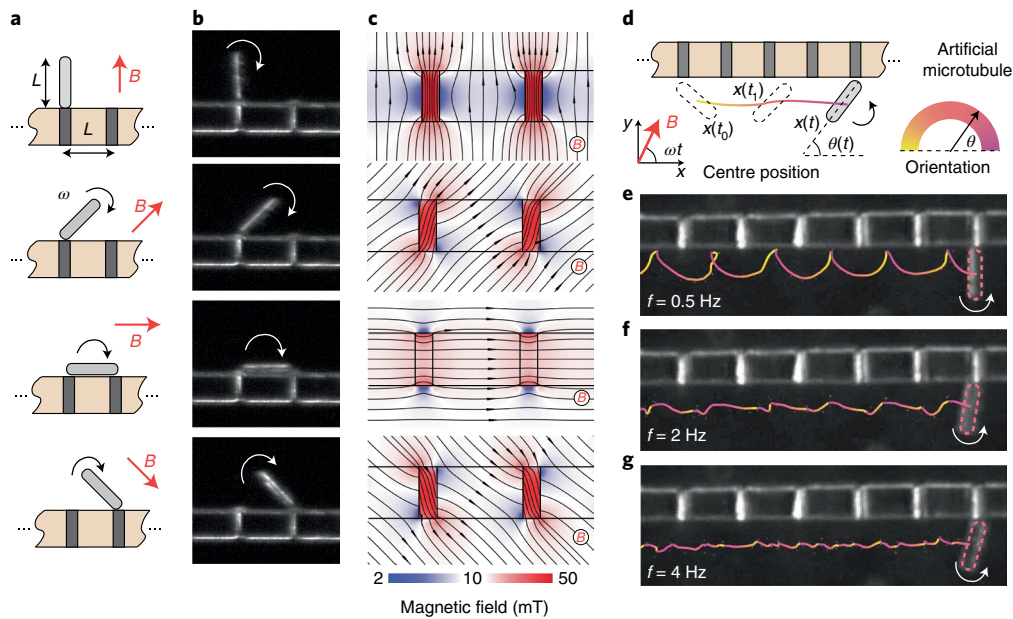


Fig. 2 | Transport of single magnetic particles on the artificial microtubule. **a, b**, Illustration (**a**) and optical images (**b**) of the basic steps of a rotating magnetic microrod on the AMT. Under a slowly rotating magnetic field B , the magnetic microrod was aligned with the external magnetic field and anchored on the stepping stones (nickel plates) to propel forwards. The microrod could walk two steps forward per cycle. The length of the microrod L is $90\ \mu\text{m}$. **c**, Numerical simulation of the magnetic field around the embedded magnetic plates. The strong magnetic-field gradient provided strong anchoring points for the magnetic microrod. **d**, Dynamic response of a walking microrod on the AMT. The centre position and orientation θ of the microrod were tracked. **e-g**, Trajectory of the microrod at external magnetic-field frequencies (f) of 0.5 Hz (**e**), 2 Hz (**f**) and 4 Hz (**g**). The colour indicates the orientation of the microrod from 0° to 180° as shown in **d**.

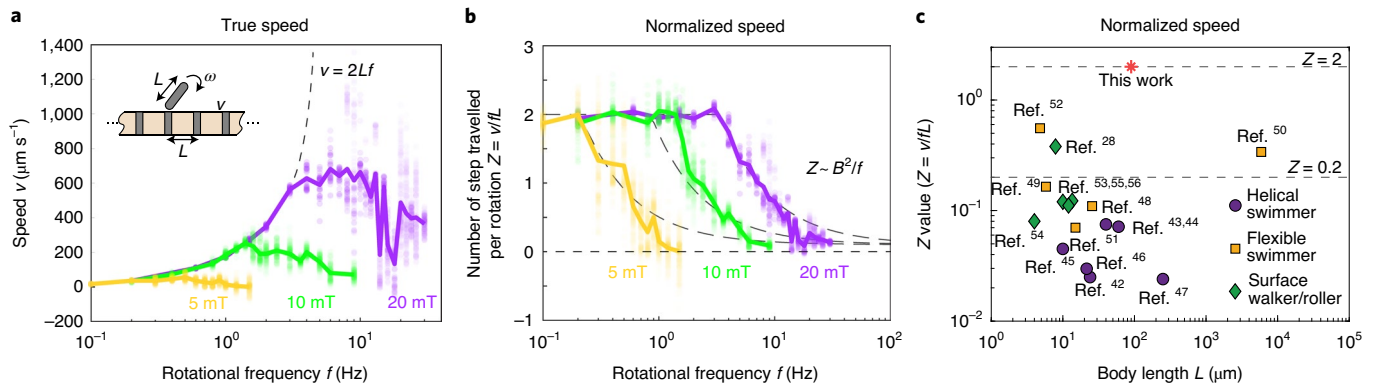


Fig. 3 | Locomotion speed on an AMT at different magnetic-field strengths and rotational frequencies. **a**, Translational speed measured for a single microrod subject to an in-plane rotating magnetic field. Three different magnetic-field strengths (5 mT in yellow, 10 mT in green and 20 mT in purple) and 99% glycerol (1.15 Pa s) were used for the experiments. Each semi-transparent round dot represents an individual speed measurement from the experimental videos and the average speed is connected with solid lines. **b**, Number of body lengths per rotation ($Z = v/fL$) for the microrod using the same measurements as in **a**. The predictions from the theoretical model (Supplementary Information) are plotted with dashed lines. **c**, Comparison of the Z value (number of body lengths travelled per rotation) for various magnetic microrobotic transport methods. Helical swimmers⁴²⁻⁴⁷, flexible swimmers⁴⁸⁻⁵² and surface walker/rollers^{28,53-56} were selected as three distinct types of magnetically driven mobile microrobot. Most reported microrobots have Z values lower than 0.2, whereas the magnetic microrods can travel on the AMT with $Z = 2$.

different magnetic-field strengths ($B = 5\ \text{mT}$, $10\ \text{mT}$ and $20\ \text{mT}$) and different frequencies ranging from 0.1 Hz to 30 Hz. The measured velocities are shown in Fig. 3a. As expected, we see that larger frequencies and stronger magnetic fields result in much faster velocities (Supplementary Video 3). Speeds of up to $1,200\ \mu\text{m s}^{-1}$ were achieved, despite the viscosity being 10^3 times larger than water. However, these curves feature a maximum, where higher frequencies lead to lower speeds. To understand this dynamic behaviour,

we defined a non-dimensionalized number, $Z = v/fL$, the number of body lengths the microrod travels per rotation, where v is the translational speed, f is the frequency of the external rotating magnetic field and L is the length of the microrod. We then plotted the same results in terms of Z in Fig. 3b. Two distinct regimes were observed. At low frequencies, the number of steps per rotation remained constant at $Z = 2$. After a critical slip-out frequency, the Z value decreased below 2 with increasing frequency. We developed a model

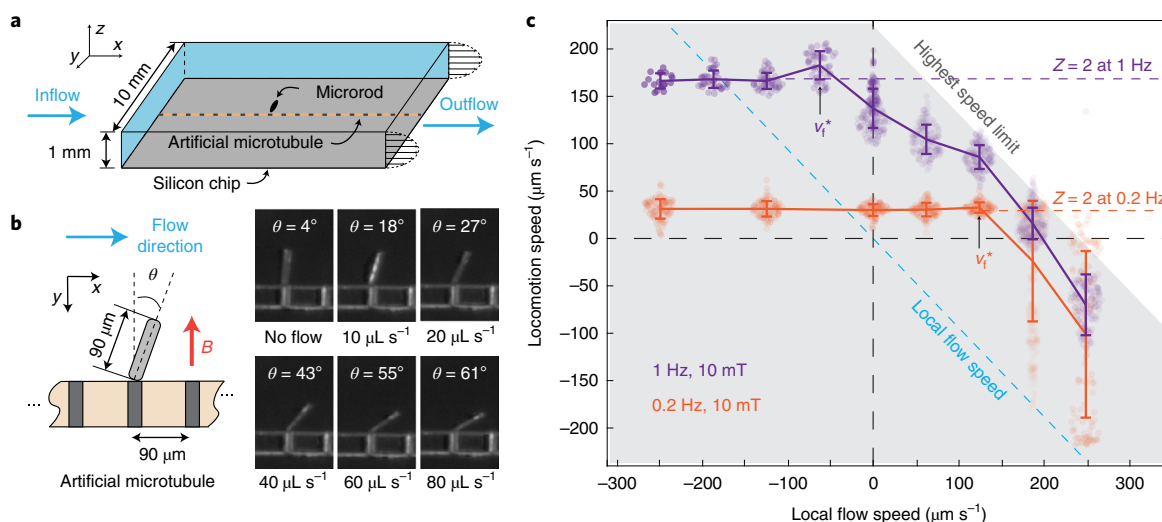


Fig. 4 | Locomotion under external fluid flow. **a**, Illustration of the experimental set-up. The AMT was fixed on the silicon chip at the bottom, and the flow was parallel to the AMT direction with a typical parabolic flow profile between two parallel plates. 99% glycerol was used for all experiments. **b**, Static anchoring capability of a microrod on the AMT under the flow. A 10 mT static magnetic field was applied perpendicular to the AMT providing a strong magnetic attraction between the microrod and the embedded magnetic plate. The equilibrium angle θ is shown for different flow strengths, where the hydrodynamic torque balances the magnetic torque. **c**, Locomotion speed of the microrod on AMTs under externally driven fluid flows. Each semi-transparent round dot represents an individual speed measurement from the experimental videos and the average speed is connected with solid lines. The positive flow rate represents movement against the flow. The speed was measured in the x direction with the particle rotating in the x - y plane (error bars, s.d.). The estimated local flow speed at the position of the microrod is plotted with a dashed blue line.

to explain the slip-out behaviour (Supplementary Information and Extended Data Fig. 3), predicting the optimal frequency. In Fig. 3b, the model results are shown as dashed lines for the different field strengths, which agree well with the experiments. Importantly, compared with existing magnetic microrobots (helical swimmers, flexible swimmers and surface rollers), our microrod has a remarkably higher Z value on the AMTs under the same magnetic actuation conditions (Fig. 3c). The strong magnetic interactions between the AMTs and the microrod allow for unseen high-speed transport at the microscale, identical to the highways formed by natural microtubules. In lower-viscosity media comparable to water, the slip-out frequency increases, allowing for even faster transport.

Locomotion and tethering under external flow

Even under strong external fluid flow, the AMTs are capable of holding magnetic particles in position and transporting them against the flow (Supplementary Video 4). Using the set-up depicted in Fig. 4a, we applied an externally driven flow in the x direction, parallel to the microtubule, which itself was fixed on the silicon substrate. Under a static magnetic field (10 mT in the y direction), the microrods were able to resist the flow by magnetically anchoring onto a stepping stone (Fig. 4b). We demonstrated that the anchor is robust to strong flows of $80 \mu\text{L s}^{-1}$, which corresponds to a local flow velocity of $v_f \approx 1,000 \mu\text{m s}^{-1}$, even when using 99% glycerol, giving a large hydrodynamic drag.

When a rotating magnetic field (10 mT in the x - y plane) was applied, the microrods were still able to walk up and down the AMT despite the flow (Fig. 4c). When moving against the flow, the microrods suffer an additional translational drag force that slows their locomotion. Similar to the stalling force of a molecular motor⁷, we identified a stalling flow rate where the speed of the microrod is zero when $v_f \approx 190 \mu\text{m s}^{-1}$. To more deeply understand this, we modified our theoretical model to account for the external flow (see 'Dynamics under the external flow' in Supplementary Information). Here we showed that the dynamics can be predicted in terms of a critical flow velocity, v_f^* , which depends on the magnetic-field strength and

frequency (marked in Fig. 4c). In weak flow, the microrobots move with a constant speed, unperturbed and robustly over a broad range of flows, with $Z=2$ when $v_f < v_f^*$. In counterflows stronger than v_f^* , the particles slow down because their Z value decreases, until they are eventually advected downstream, as expected. Interestingly, this asymmetric response to positive and negative flows can be used to develop a diode functionality, where oscillatory flows lead to net microrobot motion in one direction.

Self-assembly and collective motion of microparticles

Finally, we observed the self-assembly and subsequent collective motion of microparticles along the AMT (Fig. 5). Instead of microrods, we considered superparamagnetic composite microparticles (polystyrene with embedded Fe_3O_4 nanoparticles, average diameter $10 \mu\text{m}$). By applying an external magnetic field (20 mT rotating in the x - y plane), the particles were attracted to the stepping stones owing to the local magnetic-field gradient, and assembled into clusters (Fig. 5b, left, and Supplementary Video 5). This assembly process gradually attracted all nearby particles and accumulated them close to the AMT. Then, on reaching a critical size, the clusters became motile (Fig. 5b, right, and Supplementary Video 5). This collective motion is inherently related to the local particle density; sparse clusters remain bound to their assembly site (Fig. 5c, faint vertical lines), while dense clusters are able to bridge from one stepping stone to the next (Fig. 5c, bright diagonal lines). This effect is partially attributed to magnetic interactions, but also hydrodynamic interactions, where the flow generated by one forced particle can also push the next particle forwards. Figure 5d quantifies this transition from non-motile individual particles to propelling active clusters, showing a critical density around 200 (relative particle density). Moreover, as shown in Extended Data Fig. 8c and Supplementary Video 6, the assemblies have a higher speed with higher local concentration ($Z=2$), while smaller clusters have a lower speed ($Z=1$). Overall, the collective motion provides a shared functionality, because it minimizes the drag force per microparticle. To conclude, we demonstrate targeted delivery of numerous microparticles in a

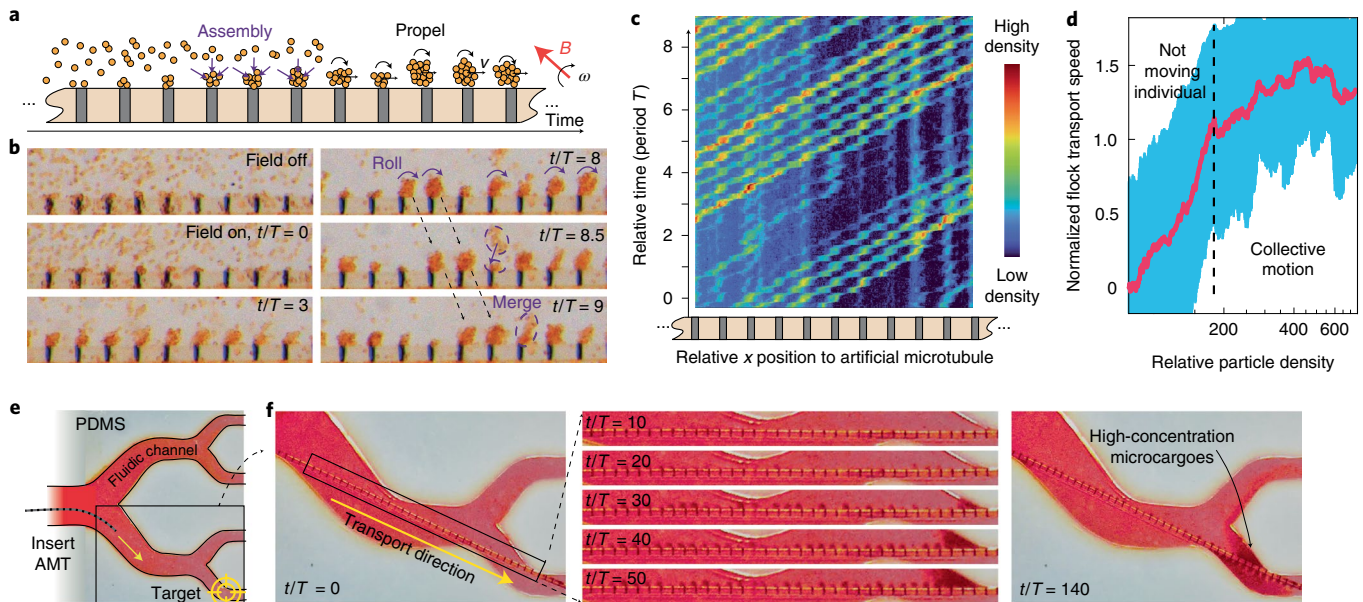


Fig. 5 | Self-assembly and collective motion along the AMT. **a**, Illustration of transport of clusters of magnetic microparticles (polystyrene with embedded Fe_3O_4 nanoparticles, average diameter $10\ \mu\text{m}$). Under a rotating magnetic field, the microparticles first assembled in a cluster and then propelled together along the AMT. **b**, Images of microparticle assembly and collective motion at different time steps. **c**, Time evolution diagram of the microparticle density close to the AMT. The bright diagonal stripes show that high-density clusters move forwards, while faint vertical stripes show that low-density clusters do not move. To match the phases of the rotating cycles, we divide time t by the rotation period T of the external magnetic field. **d**, The local transport speed of microparticle assemblies as a function of the relative particle density (see ‘Density analysis in the active cluster transport experiments’ in Methods). The pink line is the rolling average of the nearest 100 measurements, and the blue region represents the standard deviation. The speed is normalized by the driving frequency times the stepping stone separation, $v/\omega l$. **e**, Demonstration of cargo delivery in a microfluidic network. First, the AMT is guided magnetically into the branch close of the target location (yellow crosshairs). Time-lapse images then show that the microcargos move along the AMT and accumulate at the target (dark colour). See Supplementary Video 7.

microfluidic network (Fig. 5e and Supplementary Video 7). First, the AMT is guided into the fluidic branch close to the target. After applying the rotating magnetic field, clusters of microparticles are continuously propelled along the AMT and accumulated at the target site at a high concentration.

Discussion

AMTs provide a bioinspired strategy for fast, confined and guided transport of magnetic microcargoes in complex physiological conditions. They overcome the intrinsic limitations of tubular catheters and freely swimming microrobots, opening up opportunities for robust and precise cargo delivery^{30–33}. In the future, they can be combined with existing technologies; an AMT can be guided out of a microcatheter so that narrower microvascular channels can be reached. In addition, microswimmers can be guided along AMTs before swimming the last stretch independently. Our design can be implemented at different scales to match the cargo dimensions for different application scenarios, including drug delivery^{14,15,18}, magnetic tweezers^{34,35}, lab-on-a-chip applications^{36,37} and reconstituted cytoplasmic streaming³⁸. Besides transport, AMTs can offer a method for separating microparticles by size, because the particles must be large enough to bridge between the embedded stepping stones, which may be useful in confinement geometries where gravitational separation is difficult. By introducing a gradient in the stepping stone separations, a broad range of particle sizes can be separated simultaneously. Similarly, one can assemble clusters of microparticles of a specific size, using the strong local magnetic-field gradients produced by the AMTs for high-throughput processing of composite microparticles³⁹. This system may also shed light on collective particle transport

on biological microtubules. As predicted by Margaretti et al.^{40,41}, molecular motors speed up significantly at high densities because of hydrodynamic coupling. We now provide experimental evidence of this, where the microparticles indeed move faster along the AMTs at high densities. This principle of collective drag reduction will probably be important for the optimization of numerous microbiological pathways for intracellular transport.

Methods

Fabrication of artificial microtubules. The AMTs were fabricated using a photolithography-based microfabrication process on four-inch silicon wafers. A schematic illustration of the complete fabrication process is shown in Extended Data Fig. 1a.

There were four main subprocesses in the fabrication of the AMTs. First, a 400 nm silicon dioxide layer was grown on the silicon wafer through wet oxidation. This layer was removed at the very end of the process to release the samples (steps 1 and 2 in Extended Data Fig. 1a).

Second, we patterned a conductive seed layer for electroplating nickel plates (steps 3–5 in Extended Data Fig. 1a). To pattern this seed layer, we first spin coated (2,500 rpm for 30 s) a thin layer of negative photoresist (AZ nLOF 2070), baked for 2 min at 100 °C, exposed to an ultraviolet lamp (4.4 mW cm⁻² at 365 nm wavelength for 43 s) through a printed film mask (JD Photo Data), developed with alkaline developer (2.38% tetramethylammonium hydroxide solution), and rinsed with deionized water. After drying, 10 nm titanium and 200 nm gold were deposited on the patterned wafer using thermal evaporation in a vacuum chamber. The AZ photoresist was then removed in acetone together with unwarranted metal deposition.

The third subprocess was to pattern SU-8 photoresist as the structural material of AMTs. We used the processing parameters recommended in the user manual of SU-8 3025 (Kayaku Advanced Materials). A spin-coating speed of 600 rpm (for 60 s) was used to achieve a thickness of 65 μm at the centre. The soft baking time was 30 min at 95 °C, and the ultraviolet exposure dose of 250 mJ cm⁻² achieved the best geometry for the holes where nickel was later deposited. After developing, oxygen plasma (Diener plasma asher) was used to clean the sample surface

(0.5 mbar, 100 W for 20 min). The wafer was then hard baked (170 °C for 20 min) on a hotplate to improve the bonding between the SU-8 and the substrate. A poor adhesion of the SU-8 structure can be problematic during electroplating.

The fourth subprocess was to electroplate nickel inside the empty holes in the microtubule fibre. The electroplating solution was composed of nickel(II) sulfate hexahydrate 300 g l⁻¹ and boric acid 50 g l⁻¹ with deionized water. Before the deposition, the samples were immersed in the isopropyl alcohol (IPA) and water for 30 s and 5 min, respectively, to dissolve the bubbles that were trapped in the holes. Nickel was electrodeposited through an externally controlled current source (Autolab Aut83866 potentiostat/galvanostat instrument) at 50 °C with a magnetic bar constantly spinning at the bottom of the beaker. A constant current (400 A m⁻²) was applied between a nickel plate (anode) and the wafer (cathode), which were placed in parallel inside the electroplating bath. The thickness of the nickel was controlled by the electroplating time. In some cases where the electroplating time was too short or too long, the holes were not filled or overplated resulting in 'mushroom like' structures, as shown in Extended Data Fig. 1b. Finally, the silicon dioxide layer was etched by HF solution to release the samples. The samples were thoroughly washed, dried and sealed in a sample case to prevent oxidation. As in Fig. 1c, an artificial microtubule is displayed with a G25 needle (Sterican 25G x 5/8', Braun).

Fabrication of magnetic microrod. The microrod was fabricated using a similar process to that used for the microtubule. First, 10 nm titanium and 200 nm gold layers were deposited on a silicon wafer as the seed layer. Then, 10-µm-thick photoresist (AZ nLOF 2070) was patterned on the seed layer using a standard process. After rinsing with water, the wafer was electroplated with nickel using the same set-up as for the AMT. After electroplating, the AZ photoresist was removed using acetone. Microrods (15 µm in width, 90 µm in length and 8 µm in thickness) were picked off on-demand from the wafer using a microneedle.

Experimental set-up for microrod transport. To test the transport of microrod on the AMT, we fixed the microtubule on a clean silicon wafer with epoxy glue. The long axis of the nickel plates was oriented parallel to the silicon substrate, exposing both ends to the liquid and the microrod during the experiments. Considering the strong magnetic interactions between the microrod and the AMT, we purposely used 99% glycerol (ABCR, viscosity 1.15 Pa s) as a highly viscous Newtonian liquid to ensure that the dynamics were fully disclosed at low frequency (<50 Hz). The high viscous drag force on the microrod eases the micromanipulation of the microrod, and avoids the use of a high-speed camera to track the particle trajectory.

The external rotating magnetic field was applied using an eight-coil electromagnetic system (MFG-100, MagnebotiX). A uniform magnetic field was applied in the workspace. All experiments were performed at room temperature.

In the experiments where an external-pressure-driven flow was applied (Fig. 4), we used a different experimental set-up. First, a polydimethylsiloxane (PDMS) cover was cured in a precisely machined aluminium mould. After peeling off the PDMS cover, the silicon chip was assembled into the PDMS cover and bonded with a glass substrate. The height (1 mm) of the microfluidic channel was controlled by the step height machined in the aluminium mould. An inlet and outlet were punched on the PDMS and connected to flexible vinyl tubes (Masterflex Transfer Tubing, 1/16' inner diameter x 1/8' outer diameter) with needles with Luer locks (18G, Darwin Microfluidics). The flow was controlled by the syringe pump (neMESYS base and low-pressure syringe pump module, CETONI) and a constant volumetric flow rate was selected.

Particle tracking. To track the speed and orientation of the microrod, we used the Motion-Based Multiple Object Tracking (Computer Vision Toolbox, MATLAB, MathWorks). After the moving microrod was detected, the property of the tracked object was analysed using the Image Processing Toolbox in MATLAB. Both the orientation and central position of the moving microrod were obtained. The detailed tracked position and orientation are shown in Extended Data Fig. 4.

Finite element method (FEM) simulations. We used COMSOL Multiphysics to study the magnetic flux density generated around the AMT under an external magnetic field, as shown in Fig. 2c. Considering the time for magnetization (roughly microseconds) is significantly shorter than the rotating period (0.03 s at 30 Hz), we simulated the magnetic field in static conditions. On the basis of the vibrating sample magnetometer (VSM) testing results of the electroplated nickel (Extended Data Fig. 2), we assumed that the magnetization was linearly dependent on the external magnetic field, with the relative magnetic permeability equal to 23. A global uniform magnetic-field strength of 10 mT was applied to the workspace in different directions, and the corresponding magnetic flux density (*B*) maps were shown in the *x*-*y* cut plane at the middle of the microtubule structure.

We also simulated the flow profile in the set-up in Fig. 4a. A constant flow rate was applied through the inlet plane and outlet plane, as shown in Extended Data Fig. 6, and 0 Pa was given as a reference pressure on the outlet plane. No-slip boundary conditions were implemented for all surfaces. Owing to the high viscosity of the glycerol and the small geometry, the flow was quickly developed as laminar flow between the two plates. The local flow speed was proportional to

the externally driven flow rate. We measured the average flow speed next to the microtubule where the microrod was walking. The estimated speed was about 200 µm s⁻¹ at 20 µl s⁻¹, which is very similar to the measured particle drifting speed when it is on the 'slip-mode' in Extended Data Fig. 7.

Details of the active cluster experiments. We used polystyrene microparticles (micromer-M, 08-02-104, Micromod Partikeltechnologie) with embedded magnetite nanoparticles (composite particle magnetization 4.8 Am² kg⁻¹). The magnetic microparticles are monodispersed with an average diameter of 10 µm. The surfaces of the microparticles are decorated with -COOH groups for good dispersity in water solution.

The procedures for the active cluster experiments were similar to those for the microrods, with only a few differences. First, the testing medium was water. The microparticles were diluted in the deionized water to reach a lower density and then applied onto the AMT. Instead of using the silicon substrate, we fixed the AMT onto a polymer substrate to prevent unwanted light reflection. We waited until most magnetic microparticles sedimented to the bottom, and then started to apply a 20 mT uniform magnetic field rotating in the *x*-*y* plane. The images in Fig. 5b are digitally modified to enhance visibility.

In the demonstration of particle delivery in a microfluidic network shown in Fig. 5e,f, PDMS (SYLGARD 184, Dow) was moulded on microfabricated microfluidic channels. Artificial colour (rhodamine B, R6626-100G, Sigma Aldrich) was added to the deionized water. The artificial microtubule is first inserted into the targeted location and an in-plane rotating magnetic field at 20 mT. The same polystyrene microparticles (micromer-M, 08-02-104, Micromod Partikeltechnologie) are continuously delivered to the targeted location and accumulated there.

Density analysis in the active cluster transport experiments. We studied the active clustering dynamics by tracking the particle density in the vicinity of the AMT. To evaluate the particle density, we tracked pixel brightness in the region from the surface of the AMT to 50 µm off the surface. From this region, the magnetic-field gradient generated by the nickel plates was negligible. Microparticles were self-assembled into chains, and rotated around their geometric centre without translation (Supplementary Video 5). By adding all the pixel brightness values along the *y* direction at each frame, we obtained the density evolution diagram along the AMT with time. As shown in Fig. 5c, the tilted strips show the transition of the flocking particles along the AMT, while vertical lines show that the particles stay at one plate without horizontal transport.

In flock transport, we observed a collective microparticle locomotion, that is, the small blob of microparticle assembly tended to stay at the same plate while the large blob of microparticle assemblies were able to rotate to the next nickel plate. To understand this density-dependent transport, we analysed the data shown in Fig. 5c, and analysed the local flock transport speed by tracking density evolution within a half rotation cycle (1 s for 0.5 Hz) at each nickel plate. To track the particle assembly motion, we identified the peak density position by fitting a sine curve with the same periodicity, and assumed the peak of the curve was the flock position. Then, we fitted a linear curve of the peak-time plot within a cycle and used the slope of the fitted curve as the local flock particle transport speed.

Data availability

All data are available in the main text or the Supplementary Information.

Code availability

All the relevant code used to generate the results in this paper and Supplementary Information is available upon request.

Received: 20 January 2022; Accepted: 14 June 2022;

Published online: 21 July 2022

References

- Phillips, R., Kondev, J., Theriot, J. & Garcia, H. *Physical Biology Of The Cell* (Garland Science, 2012).
- Elgeti, J., Winkler, R. G. & Gompper, G. Physics of microswimmers—single particle motion and collective behavior: a review. *Reports Prog. Phys.* **78**, 056601 (2015).
- Needleman, D. & Dogic, Z. Active matter at the interface between materials science and cell biology. *Nat. Rev. Mater.* **2**, 17048 (2017).
- Ramirez-San Juan, G. R. et al. Multi-scale spatial heterogeneity enhances particle clearance in airway ciliary arrays. *Nat. Phys.* **16**, 958–964 (2020).
- Hirokawa, N., Noda, Y., Tanaka, Y. & Niwa, S. Kinesin superfamily motor proteins and intracellular transport. *Nat. Rev. Mol. Cell Biol.* **10**, 682–696 (2009).
- Schliwa, M. & Woehlke, G. Molecular motors. *Nature* **422**, 759–765 (2003).
- Visscher, K., Schnitzer, M. J. & Block, S. M. Single kinesin molecules studied with a molecular force clamp. *Nature* **400**, 184–189 (1999).
- Goldstein, R. E. & van de Meent, J.-W. A physical perspective on cytoplasmic streaming. *Interface Focus* **5**, 20150030 (2015).

9. Chen, L., Nakamura, M., Schindler, T. D., Parker, D. & Bryant, Z. Engineering controllable bidirectional molecular motors based on myosin. *Nat. Nanotechnol.* **7**, 252–256 (2012).
10. Kassem, S. et al. Artificial molecular motors. *Chem. Soc. Rev.* **46**, 2592–2621 (2017).
11. Fredy, J. W. et al. Molecular photoswitches mediating the strain-driven disassembly of supramolecular tubules. *Proc. Natl Acad. Sci. USA* **114**, 11850–11855 (2017).
12. Cheng, S., Aggarwal, A. & Stevens, M. J. Self-assembly of artificial microtubules. *Soft Matter* **8**, 5666–5678 (2012).
13. Lubbe, A. S., Wezenberg, S. J. & Feringa, B. L. Artificial microtubules burst with energy. *Proc. Natl Acad. Sci. USA* **114**, 11804–11805 (2017).
14. Nelson, B. J., Kaliakatos, I. K. & Abbott, J. J. Microrobots for minimally invasive medicine. *Annu. Rev. Biomed. Eng.* **12**, 55–85 (2010).
15. Li, J., de Ávila, B. E.-F., Gao, W., Zhang, L. & Wang, J. Micro/nanorobots for biomedicine: delivery, surgery, sensing, and detoxification. *Sci. Robot.* **2**, eaam6431 (2017).
16. Goel, A. & Vogel, V. Harnessing biological motors to engineer systems for nanoscale transport and assembly. *Nat. Nanotechnol.* **3**, 465–475 (2008).
17. Rosenblum, D., Joshi, N., Tao, W., Karp, J. M. & Peer, D. Progress and challenges towards targeted delivery of cancer therapeutics. *Nat. Commun.* **9**, 1410 (2018).
18. Schmidt, C. K., Medina-Sánchez, M., Edmondson, R. J. & Schmidt, O. G. Engineering microrobots for targeted cancer therapies from a medical perspective. *Nat. Commun.* **11**, 5618 (2020).
19. Cui, J., Huang, T., Luo, Z., Testa, P. & Gu, H. Nanomagnetic encoding of shape-morphing micromachines. *Nature* **575**, 164–168 (2019).
20. Palagi, S. et al. Structured light enables biomimetic swimming and versatile locomotion of photoresponsive soft microrobots. *Nat. Mater.* **15**, 647–653 (2016).
21. Zhang, L. et al. Artificial bacterial flagella: fabrication and magnetic control. *Appl. Phys. Lett.* **94**, 64107 (2009).
22. Ghosh, A. & Fischer, P. Controlled propulsion of artificial magnetic nanostructured propellers. *Nano Lett.* **9**, 2243–2245 (2009).
23. Servant, A., Qiu, F., Mazza, M., Kostarelos, K. & Nelson, B. J. Controlled in vivo swimming of a swarm of bacteria-like microrobotic flagella. *Adv. Mater.* **27**, 2981–2988 (2015).
24. Huang, T.-Y., Gu, H. & Nelson, B. J. Increasingly intelligent micromachines. *Annu. Rev. Control. Robot. Auton. Syst.* **5**, 279–310 (2022).
25. Ahmed, D. et al. Bioinspired acousto-magnetic microswarm robots with upstream motility. *Nat. Mach. Intell.* **3**, 116–124 (2021).
26. Yang, T. et al. Microwheels on microroads: enhanced translation on topographic surfaces. *Sci. Robot.* **4**, eaaw9525 (2019).
27. Wang, Q. et al. Ultrasound Doppler-guided real-time navigation of a magnetic microswarm for active endovascular delivery. *Sci. Adv.* **7**, eaab5914 (2021).
28. Alapan, Y., Bozuyuk, U., Erkoc, P., Karacakol, A. C. & Sitti, M. Multifunctional surface microrollers for targeted cargo delivery in physiological blood flow. *Sci. Robot.* **5**, eaab5726 (2020).
29. Wang, B. et al. Endoscopy-assisted magnetic navigation of biohybrid soft microrobots with rapid endoluminal delivery and imaging. *Sci. Robot.* **6**, eaab2813 (2021).
30. Pancaldi, L. et al. Flow driven robotic navigation of microengineered endovascular probes. *Nat. Commun.* **11**, 6356 (2020).
31. Vitiello, V., Lee, S.-L., Cundy, T. P. & Yang, G.-Z. Emerging robotic platforms for minimally invasive surgery. *IEEE Rev. Biomed. Eng.* **6**, 111–126 (2012).
32. Kim, Y., Parada, G. A., Liu, S. & Zhao, X. Ferromagnetic soft continuum robots. *Sci. Robot.* **4**, eaax7329 (2019).
33. Azizi, A., Tremblay, C. C., Gagné, K. & Martel, S. Using the fringe field of a clinical MRI scanner enables robotic navigation of tethered instruments in deeper vascular regions. *Sci. Robot.* **4**, eaax7342 (2019).
34. Neuman, K. C. & Nagy, A. Single-molecule force spectroscopy: optical tweezers, magnetic tweezers and atomic force microscopy. *Nat. Methods* **5**, 491–505 (2008).
35. Gosse, C. & Croquette, V. Magnetic tweezers: micromanipulation and force measurement at the molecular level. *Biophys. J.* **82**, 3314–3329 (2002).
36. Moerland, C. P., Van IJendoorn, L. J. & Prins, M. W. J. Rotating magnetic particles for lab-on-chip applications—a comprehensive review. *Lab Chip* **19**, 919–933 (2019).
37. Katsikis, G., Cybulski, J. S. & Prakash, M. Synchronous universal droplet logic and control. *Nat. Phys.* **11**, 588–596 (2015).
38. Gong, X., Mathijssen, A.J.T.M., Bryant, Z. & Prakash, M. Engineering reconfigurable flow patterns via surface-driven light-controlled active matter. *Phys. Rev. Fluids* **6**, 123104 (2021).
39. Dendukuri, D., Pregel, D. C., Collins, J., Hatton, T. A. & Doyle, P. S. Continuous-flow lithography for high-throughput microparticle synthesis. *Nat. Mater.* **5**, 365–369 (2006).
40. Margaretti, P., Pagonabarraga, I. & Frenkel, D. Running faster together: huge speed up of thermal ratchets due to hydrodynamic coupling. *Phys. Rev. Lett.* **109**, 168101 (2012).
41. Margaretti, P., Pagonabarraga, I. & Joanny, J.-F. Bistability, oscillations, and bidirectional motion of ensemble of hydrodynamically coupled molecular motors. *Phys. Rev. Lett.* **119**, 168101 (2017).
42. Zhang, L. et al. Characterizing the swimming properties of artificial bacterial flagella. *Nano Lett.* **9**, 3663–3667 (2009).
43. Tottori, S. et al. Magnetic helical micromachines: fabrication, controlled swimming, and cargo transport. *Adv. Mater.* **24**, 811–816 (2012).
44. Peters, C. et al. Superparamagnetic twist-type actuators with shape-independent magnetic properties and surface functionalization for advanced biomedical applications. *Adv. Funct. Mater.* **24**, 5269–5276 (2014).
45. Maier, A. M. et al. Magnetic propulsion of microswimmers with DNA-based flagellar bundles. *Nano Lett.* **16**, 906–910 (2016).
46. Medina-Sánchez, M., Schwarz, L., Meyer, A. K., Hebenstreit, F. & Schmidt, O. G. Cellular cargo delivery: toward assisted fertilization by sperm-carrying micromotors. *Nano Lett.* **16**, 555–561 (2016).
47. Huang, T.-Y. et al. 3D printed microtransporters: Compound micromachines for spatiotemporally controlled delivery of therapeutic agents. *Adv. Mater.* **27**, 6644–6650 (2015).
48. Dreyfus, R. et al. Microscopic artificial swimmers. *Nature* **437**, 862–865 (2005).
49. Pak, O. S., Gao, W., Wang, J. & Lauga, E. High-speed propulsion of flexible nanowire motors: theory and experiments. *Soft Matter* **7**, 8169–8181 (2011).
50. Diller, E., Zhuang, J., Zhan Lum, G., Edwards, M. R. & Sitti, M. Continuously distributed magnetization profile for millimeter-scale elastomeric undulatory swimming. *Appl. Phys. Lett.* **104**, 174101 (2014).
51. Jang, B. et al. Undulatory locomotion of magnetic multilink nanoswimmers. *Nano Lett.* **15**, 4829–4833 (2015).
52. Li, T. et al. Magnetically propelled fish-like nanoswimmers. *Small* **12**, 6098–6105 (2016).
53. Tasci, T. O., Herson, P. S., Neeves, K. B. & Marr, D. W. M. Surface-enabled propulsion and control of colloidal microwheels. *Nat. Commun.* **7**, 10225 (2016).
54. Tierno, P., Golestanian, R., Pagonabarraga, I. & Sagués, F. Controlled swimming in confined fluids of magnetically actuated colloidal rotors. *Phys. Rev. Lett.* **101**, 218304 (2008).
55. Sing, C. E., Schmid, L., Schneider, M. F., Franke, T. & Alexander-Katz, A. Controlled surface-induced flows from the motion of self-assembled colloidal walkers. *Proc. Natl Acad. Sci. USA* **107**, 535–540 (2010).
56. Ahmed, D. et al. Neutrophil-inspired propulsion in a combined acoustic and magnetic field. *Nat. Commun.* **8**, 770 (2017).

Acknowledgements

We thank X.-P. Wang and S. Pane for helping with the development of the fabrication process. We thank X. Chen for his help on the VSM test and E. Zuurmond for proofreading this article. The sample fabrication was performed using the cleanroom facilities at the FIRST at ETH Zurich. We thank the ETH Lab Supporting Group for the deposition process. Funding: This work was financially supported by the European Research Council Advanced Grant–Soft MicroRobots (SOMBOT, number 743217), Swiss National Science Foundation grant 200020B_185039 and an ETH grant (1916-1).

Author contributions

H.G. conceived the idea and managed the research. E.H., H.G. and T.-Y.H. fabricated the artificial microtubules. H.G. and E.H. performed the experiments and analysed the data. A.J.T.M.M. and H.G. developed the theoretical model. H.G., A.J.T.M.M. and Q.B. wrote the manuscript with contributions from all authors. B.J.N. supervised this project.

Competing interests

The authors declare no competing interests.

Additional information

Extended data is available for this paper at <https://doi.org/10.1038/s42256-022-00510-7>.

Supplementary information The online version contains supplementary material available at <https://doi.org/10.1038/s42256-022-00510-7>.

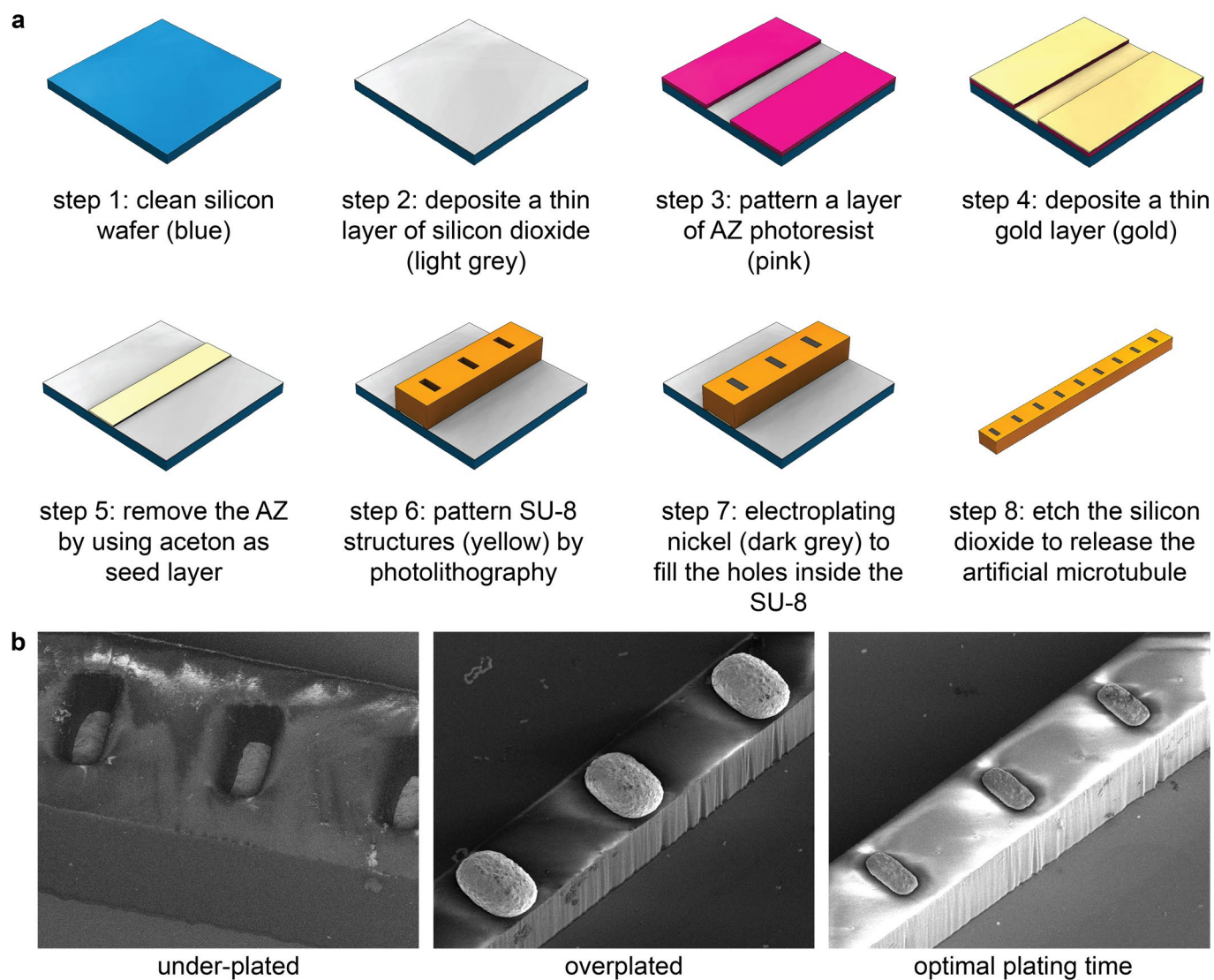
Correspondence and requests for materials should be addressed to Hongri Gu, Arnold J. T. M. Mathijssen or Bradley J. Nelson.

Peer review information *Nature Machine Intelligence* thanks Gerhard Gompper and the other, anonymous, reviewer(s) for their contribution to the peer review of this work.

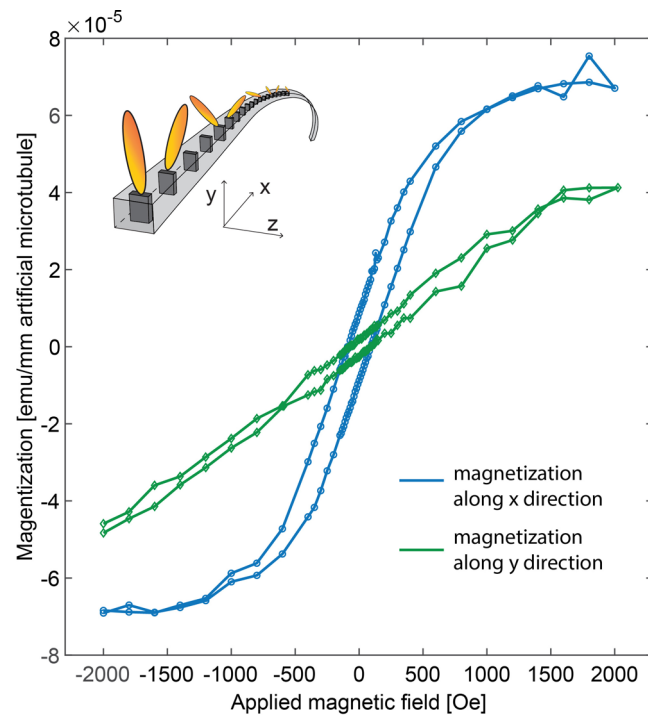
Reprints and permissions information is available at www.nature.com/reprints.

Publisher's note Springer Nature remains neutral with regard to jurisdictional claims in published maps and institutional affiliations.

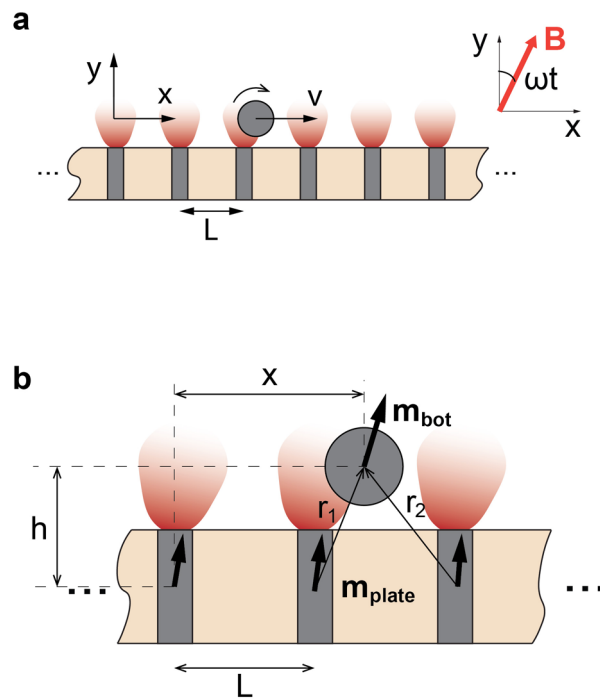
© The Author(s), under exclusive licence to Springer Nature Limited 2022



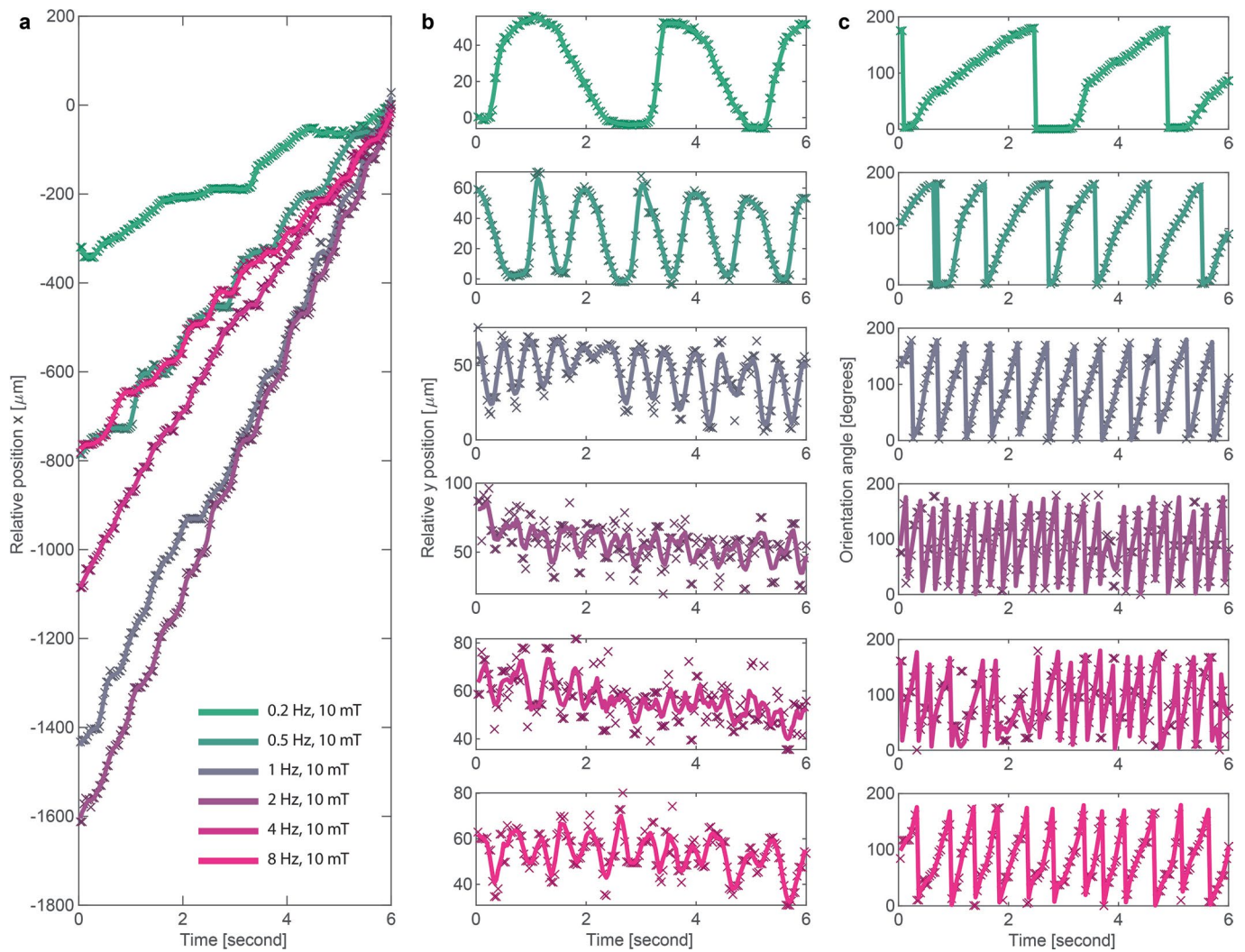
Extended Data Fig. 1 | Fabrication process of artificial microtubules. **a**, Schematic illustration of the microfabrication processes of the AMTs. The details of the microfabrication can be found in Methods: Fabrication of AMTs. **b**, SEM images of the microtubule samples with different electroplating time. Under an optimal electroplating time, the nickel plates have the same height as the SU-8 fibre.



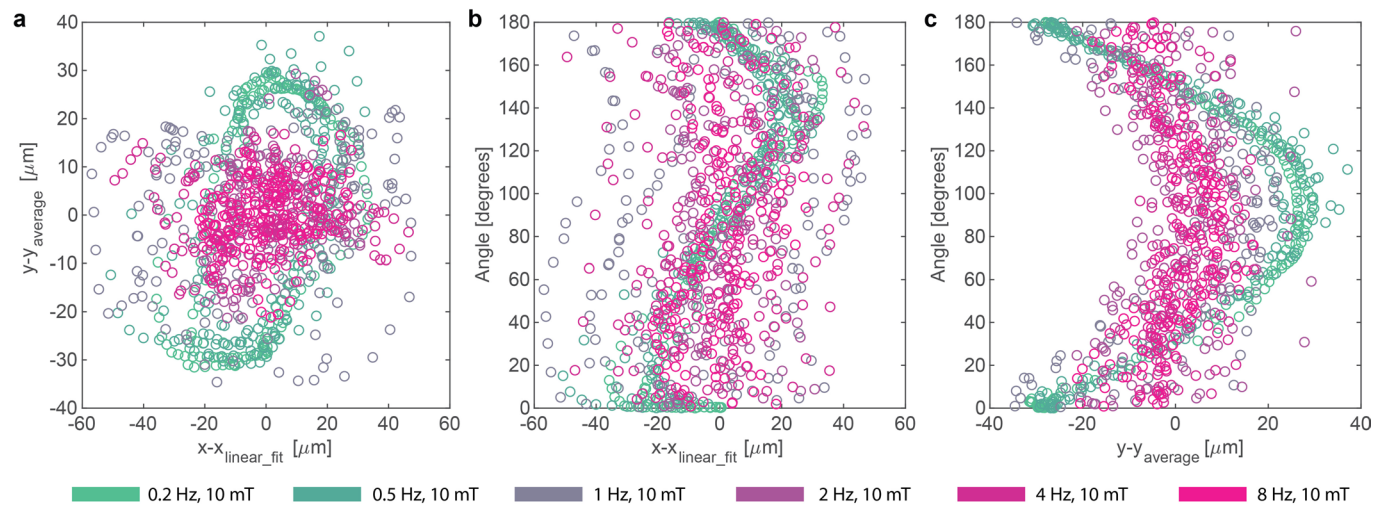
Extended Data Fig. 2 | Magnetic properties of artificial microtubules. We tested the AMT sample using the VSM. The testing sample was a segment of the AMT, with 92 embedded nickel plates with a length of 8.28 mm. The sample behaved as typical soft magnetic materials with a low coercivity of 90 Oe.



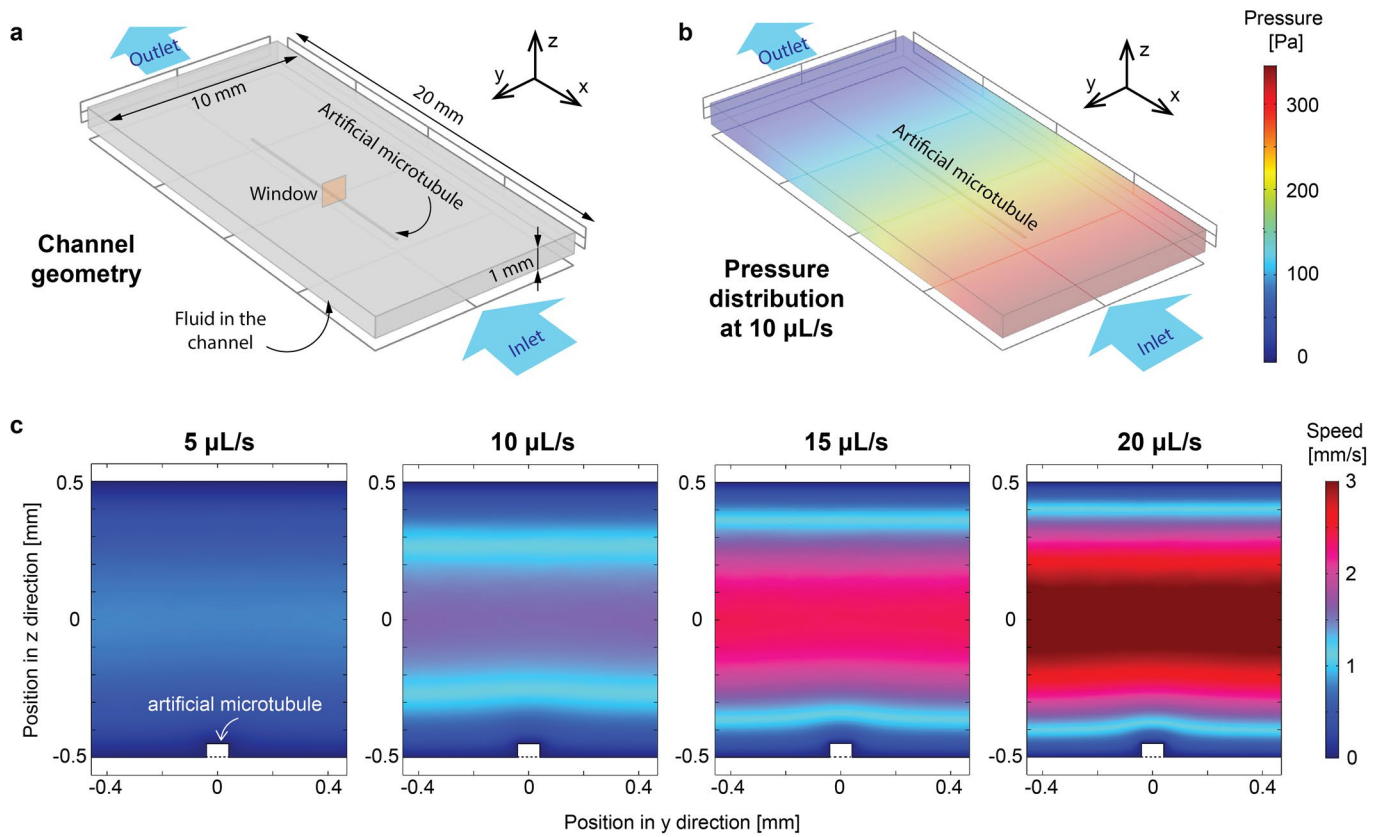
Extended Data Fig. 3 | Diagram of magnetic microrobot transport on an artificial microtubule. a, A spherical magnetic particle near the AMT. The red shaded areas represent the magnetic-field gradient. **b**, Modelling of magnetic interactions between a magnetic microrobot and embedded nickel plates.



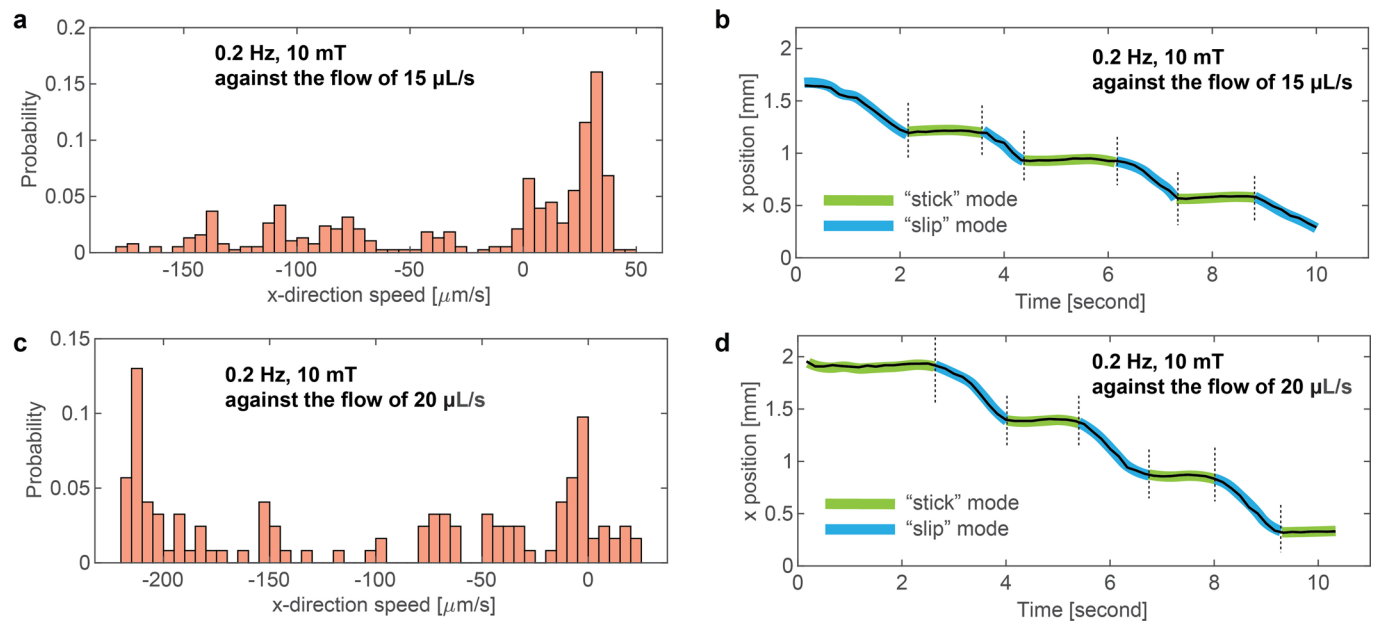
Extended Data Fig. 4 | Position and orientation tracking results of a microrod walking on AMTs. a-c, Subfigures represent the relative x, y position and the orientation angle, respectively. The tracking time frame was 6 seconds, until the microrod reached the same reference x position. The solid lines are the moving average of the nearest 5 measurements.



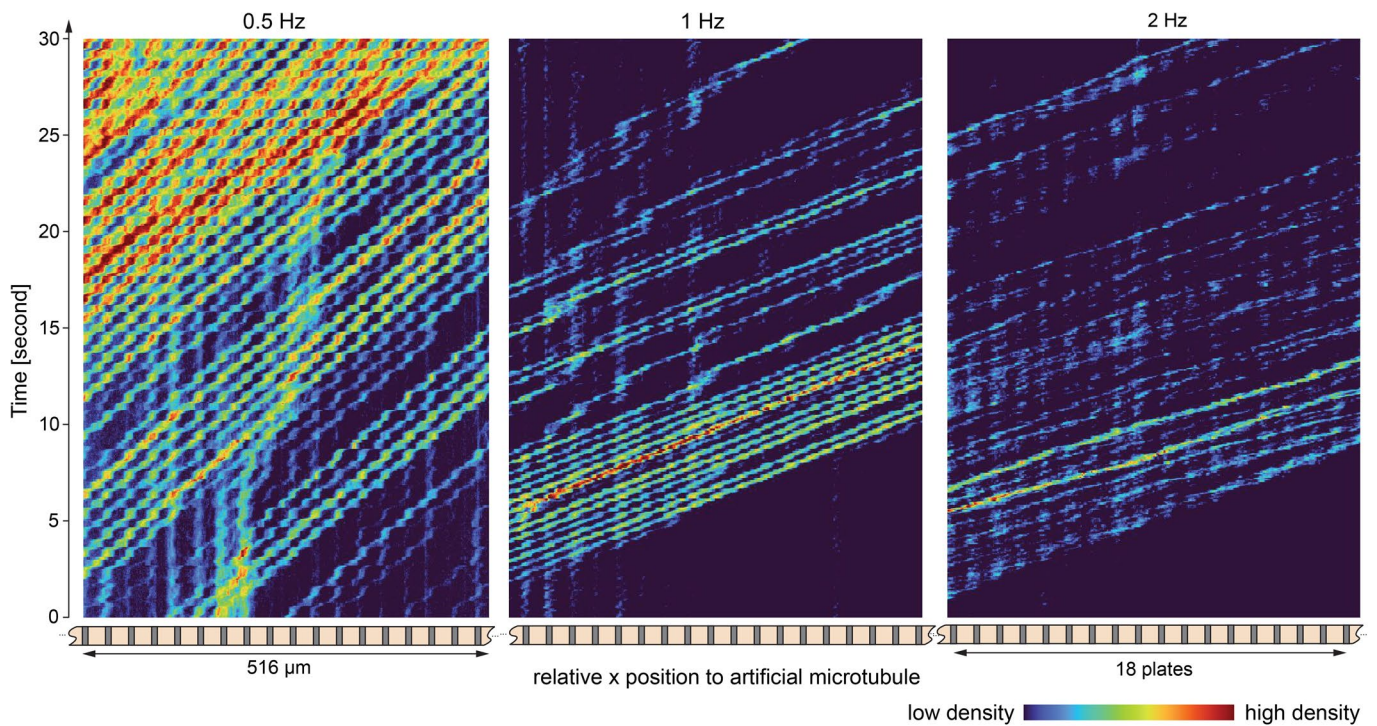
Extended Data Fig. 5 | Correlation of tracking results of x, y and angle within each period from the data used in Extended Data Fig. 4. At low frequencies there are strong correlations between x, y, and the orientation angle, due to the periodic semicircle trajectories.



Extended Data Fig. 6 | Externally driven fluidic flow simulation of the experimental set-up. **a**, Channel geometry in the FEM simulation. The microtubule was fixed at the bottom of the substrate. The inlet and outlet were far from the AMT allowing the flow to be fully developed as a typical Couette flow. **b**, Simulation of fluid pressure along the channel length. **c**, Simulation of fluid flow along the x direction in the observation window near the microtubule. The average flow speed was measured at the position where the microrod was walking. The estimated flow speed was 200 $\mu\text{m/s}$ at 20 $\mu\text{L/s}$, which agrees well with the experimental observation shown in Fig. 4c.



Extended Data Fig. 7 | ‘Stick and slip’ behaviour against strong flow under 0.2 Hz rotating magnetic field. At a low frequency of 0.2 Hz, the locomotion of the microrod is highly dependent on the magnetic-field direction within a period, showing ‘stick and slip’ behaviour, explaining the reason for the wide dispersion of the tracking speed. The video can be found in Supplementary Video 4.



Extended Data Fig. 8 | Comparison of flocking microparticle transport on the microtubules at different frequencies. The tilted stripes show the translation of the flocking particles over time, and the slope of the bright stripes represent the local transport speed. At 1 Hz, the transport was faster than at 0.5 Hz. At 2 Hz, we observed that slopes were different depending on the local density. The two bright stripes have a higher speed than the rest of the stripes.